RESEARCH ARTICLE

Nanoscale speckle patterning for combined high-resolution strain and orientation mapping of environmentally sensitive materials

Benjamin Poole[1] [iD] | Alex Marsh[1] | David Lunt[1,2] | Chris Hardie[1] |
Mike Gorley[1] | Cory Hamelin[1] | Allan Harte[1]

[1]United Kingdom Atomic Energy Authority, Culham Centre for Fusion Energy, Culham Science Centre, Abingdon, UK

[2]Department of Materials, University of Manchester, Manchester, UK

Correspondence
Benjamin Poole, United Kingdom Atomic Energy Authority, Culham Centre for Fusion Energy, Culham Science Centre, Abingdon, Oxon OX14 3DB, UK.
Email: ben.poole@ukaea.uk

Abstract

Scanning electron microscopy-based high-resolution digital image correlation (HRDIC) is now an established technique, providing full-field strain and displacement measurement at the microscale. Techniques for generating speckle patterns for sub-micron strain mapping can often be either substrate dependent or rely on applying aggressive conditions which may alter the microstructure of interest or damage the substrate in highly sensitive materials. We detail a modification of a methodology successfully applied in the literature to allow its use with metallic materials that are particularly sensitive to the corrosive media, such as copper-base alloys. Nanometre-thick silver films, applied with physical vapour deposition, are remodelled using NaBr in non-aqueous isopropanol, replacing the aqueous solution of NaCl in the original method, forming a uniform dispersion of silver islands highly suitable for digital image correlation (DIC) measurement. The entire procedure is performed at ambient temperature. We find that the DIC pattern is suitably electron transparent to allow electron backscatter diffraction (EBSD) measurements without pattern removal, producing diffraction patterns of sufficient quality for cross-correlation based high-angular resolution EBSD. This property facilitates simultaneous EBSD and DIC mapping experiments, providing deeper insights into the kinematics of plastic deformation in crystalline materials. Sub-100 nm islands are achieved through control of the sputter coating parameters, resulting in DIC cross-correlation subwindows of 140 nm with a 50% overlap. This resolution is sufficient to capture the fine detail of strain localisation phenomena during plastic deformation, demonstrated here with a case study in CuCrZr, a precipitation-hardened heat sink material for application in nuclear fusion components. Here, we extract full-field displacement data with DIC and corresponding orientation information using EBSD without the need for pattern removal.

1 | INTRODUCTION

Scanning electron microscopy (SEM)-based high-resolution digital image correlation (HRDIC) is now a well-established tool for characterising microstructurally controlled deformation behaviour in engineering alloys. HRDIC has found significant application in understanding materials relevant to power generation industries [1], in particular titanium alloys [2–4] and nickel-base superalloys [5–12] for gas turbines, steels [13–18], zirconium-base alloys [19, 20] for nuclear fission applications, refractory alloys [21] and high entropy alloys [22].

HRDIC strain mapping is dependent on the application of a suitably sized, homogeneously distributed, random speckle pattern. The applied pattern must not introduce deleterious artefacts which may mask the true deformation behaviour of the substrate. Due to the wide selection of materials of interest examined in the literature, a range of material specific patterning methodologies have been developed [23, 24].

Reviews of currently developed patterning methodologies for HRDIC show a diverse range of application techniques available for different materials [1, 23, 24]. However, there are limitations to many techniques, with those more suitable for application on delicate specimens (i.e., micro-mist nebulisation [24]) offering reduced pattern quality, whereas those resulting in high-performance patterns (i.e., gold remodelling [19, 25, 26]) utilising a more aggressive patterning environment. Patterning techniques such as the application functionalised gold nanoparticles offer high-performance patterns, are applied at room temperature and can be removed through a chemical process following testing for post-test electron backscatter diffraction (EBSD) measurements [3, 8, 27]. However, this methodology requires significant use of chemical reagents, often not available in standard metallography laboratories. Therefore, the aim of this work is to devise a technique that produces high-quality speckle patterns suitable for strain mapping at sub-micron spatial resolutions while not damaging the substrate of highly sensitive materials. An emphasis was also placed on reducing the use of potentially hazardous chemicals and specialist equipment.

Room temperature pattern application is a key requirement as many materials cannot tolerate exposure to elevated temperature or the application of temperature will alter the microstructure that we wish to study. Precipitation-hardened alloys are a prime example of this, with ageing heat treatments of similar temperatures and durations to the conditions applied during some HRDIC patterning procedures. For materials such as Al–Cu or CuCrZr (ageing heat treatments of ∼220°C and ∼480°C, respectively [28, 29]), this heating may change the nano-precipitate microstructure of interest, invalidating experimental results. Heating also precludes the use of HRDIC to study deformation of low melting point alloys, such as solders, limiting studies to EBSD examination [30–32]. Finally, the drive to examine the mechanical performance of irradiated material precludes the application of temperature for patterning purposes, as any thermal annihilation of irradiation-induced defects will change the fundamental damage structures of interest.

A secondary challenge for patterning techniques is chemical compatibility with the patterning environment. Corrosion sensitivity has already been demonstrated to be problematic for materials such as magnesium [25, 27] and zirconium-base alloys [19], leading to the formation of a surface oxide layer which masks the true deformation of the substrate. As such, chemical compatibility between the patterning reagents and the material of interest is required to prevent this effect. For many materials, this requires the use of non-aqueous conditions [8, 25, 27].

In what follows, we describe a modification to the patterning process described by Montgomery et al. [33], extending its applicability to temperature and corrosion sensitive materials through the replacement of aqueous solvents with a non-aqueous alcohol while maintaining the valuable properties of the resulting patterns. We report the properties of the speckle patterns, including its compatibility with EBSD orientation mapping. Finally, to demonstrate the successful use of this technique, we present a deformation mapping case study in peak-aged CuCrZr, including post-deformation EBSD orientation and rotation measurements without removal of the speckle pattern. This represents a challenging material test case since it exhibits both temperature and corrosion sensitivity.

2 | MATERIALS

To ensure that our pattern is suitable for sensitive materials, we examine peak-aged CuCrZr. CuCrZr is a precipitation-hardened alloy containing nanoscale chromium-rich precipitate particles within a face-centred cubic copper matrix, with a nominal composition of 0.6–0.9 wt.% chromium and 0.07–0.15 wt.% zirconium for ITER-grade material [29, 34]. To ensure that there is sufficient chromium in solid solution to form nano-precipitates, the chromium content exceeds the solubility limit in copper, leading to the formation of larger micron-scale body-centred cubic chromium precipitates within the microstructure. In the peak-aged condition, the nano-precipitates are spherical with a diameter of approximately 3 nm, achieved through a solution annealing heat treatment at ~1000°C for 30–60 minutes, followed by an ageing treatment at ~480°C for 2–4 hours [29, 34, 35].

Copper-base alloys are of key interest for fusion components, in particular for components requiring high heat transfer rates. Oxygen-free, high-conductivity copper (OFHC-Cu) is proposed as an interlayer in some divertor designs, acting as a layer between the tungsten armour facing the plasma and the CuCrZr heatsink containing coolant water [36–38]. In these monoblock designs, the copper components have an operating temperature range of approximately 150–300°C and are exposed to complex cyclic mechanical and thermal loading, fluid–structure interactions and high levels of neutron irradiation. As such, a knowledge of the deformation behaviour of this material is key to predicting performance through component life. The thermophysical and bulk mechanical properties of Cu-base alloys are well characterised [29, 34], but there is a need to understand the mechanical deformation behaviour of these alloys at the microstructural length scale and following exposure to irradiation.

While being of key relevance to fusion technology, these alloys represent challenging test cases for HRDIC analyses. Cu-base alloys readily oxidise under aqueous conditions or under the application of heat. The formation of surface oxides is known to be highly detrimental to HRDIC measurements, resulting in the strain measurements showing cracking of the surface oxide rather than deformation in the underlying substrate [19]. The application of heat during patterning is incompatible with HRDIC for ion or neutron irradiated materials as this may anneal out or alter the irradiation damage of interest, particularly if the specimen is heated above the temperature at which it was irradiated. Furthermore, this heat may lead to evolution of the precipitate microstructure [39].

Copper-base alloys are difficult to prepare, especially to a surface quality suitable for EBSD and HRDIC analyses. Electropolishing can produce significant and undesirable surface topology and edge rounding and therefore mechanical polishing was used. Specimens were ground to a P4000 finish, followed by 1 μm diamond polishing. A three-stage final etch-polish process was used to produce a flat, deformation-free surface (Table 1). Neat colloidal silica without the addition of an etchant was found to cause significant corrosion and did not remove grinding damage. Therefore, a first-stage polish using colloidal silica (MetPrep OPUS) with hydrogen peroxide and ammonia water was used to remove surface damage from earlier grinding and polishing steps. A second-stage polish using colloidal silica with only hydrogen peroxide was then used to clean the surface, removing any chemically adhered silica particles from the copper surface. Finally, a brief polish in de-ionised water was required to remove the last remnants of colloidal silica resulting in a clean, deformation-free surface suitable for speckle pattern optimisation.

TABLE 1 Final polishing routine used for OFHC-Cu and CuCrZr.

Step	Surface	Solution	Time
1	MetPrep Chemicloth	96 parts MetPrep OPUS 2 parts 3 vol.% H_2O_2 in de-ionised water 2 parts 20 vol.% NH_3 in de-ionised water	10 min
2	MetPrep Chemicloth	4 parts MetPrep OPUS 1 part 30 vol.% H_2O_2 in de-ionised water	5 min
3	MetPrep Chemicloth	De-ionised water	1 min

3 | GENERATING A SUITABLE PATTERN

3.1 | Currently available patterning methodologies

A HRDIC patterning technique must satisfy several constraints to enable successful strain measurement: sufficient contrast between the pattern and substrate, feature sizes at a suitable scale relative to the microstructural and deformation features of interest, high levels of coverage and compatibility with the substrate [26, 40].

An ideal pattern would be deposited at room temperature but remain stable at elevated temperature.

A number of patterning methodologies suitable for SEM-based HRDIC exist in the literature with the most successful typically relying on some form of thin metal film remodelling. These are ideal patterns due to the uniform distribution of the features and the high level of z-contrast with backscattered electron imaging with these patterns. Gold remodelling heats the specimen to ∼150°C or ∼300°C for styrene [19, 25] or water vapour [13, 26] based remodelling, respectively. Styrene-based remodelling may not pose a corrosion hazard to copper-base alloys, but the 150°C remodelling temperature may cause ageing of the nano-precipitates and radiation damage annealing. Stabilisation of these types of patterns for higher temperature testing also requires additional heat treatment at the experimental temperature to stop the pattern from developing further [41].

The more recent InSn one-step sputtering-remodelling technique of Hoefnagels et al. [42] shows promise since its application is conducted entirely at ambient temperature. However, the low melting point of the InSn alloy precludes any elevated temperature testing. There is also concern of the compatibility of tin with a copper specimen, with the possibility of Sn from the pattern diffusing into the Cu substrate [43]. Finally, this method requires a high-performance, high-vacuum magnetron sputter coater to allow for remodelling of the pattern in situ.

There are several other methodologies in the literature that do not use thin film remodelling. Deposition of inert particles such as silica [24, 44] does not achieve sufficient pattern density or suitably sized speckles to give the required spatial resolution in strain measurement for the finely spaced slip bands expected in copper alloys. The functionalised gold nanoparticle methodology may be compatible with delicate copper-base alloys but requires a range of chemical reagents to prepare the nanoparticles and apply them to the substrate and is also time consuming [8, 45]. Goulmy et al. [46] have used chemical etching to produce a suitable speckle pattern which is both sufficiently fine to resolve slip bands and electron translucent to allow simultaneous EBSD analysis. However, there are concerns that etching pits may alter the surface stress state, influencing the observed deformation trends.

The chemically remodelled silver film technique proposed by Montgomery et al. [33] (hereafter aqueous remodelled Ag) fulfils the room temperature application criterion and has been demonstrated to be suitable for elevated temperature testing [47]. This technique has been successively applied to multiple substrates including zirconia ceramic [33], glass fibre epoxy composites [33] and titanium alloys [33, 47, 48]. While a sublayer of Ti is suggested to protect the substrate from the relatively corrosive NaCl solution, we have found that significant corrosion still occurs in copper-base alloys, resulting in surface pitting and the formation of a poorly adhered oxide layer which readily spalls off (Figure 1). Since the corrosion issues of this technique are related to the solvent used to remodel the silver film, this method forms the basis for our new patterning technique, where a silver film is remodelled using a non-aqueous solution, compatible with sensitive substrates.

3.2 | Ti–Ag non-aqueous remodelling methodology

A key benefit of the aqueous remodelled Ag method is the ease of application and lack of the need for specialist equipment other than a sputter coater, which are readily found in most electron microscopy facilities. Silver has already been demonstrated as a suitable patterning material for HRDIC as demonstrated in the original chemical remodelling process of Montgomery et al. [33], in the water vapour remodelling followed by furnace heat treatment process of Edwards et al. [41] or as dispersed nanoparticles by Yamasaki et al. [11]. Although not intentionally applied for HRDIC, the types of silver nanoparticle patterns often used in surface enhanced ramen spectroscopy show many of the hallmarks of a good HRDIC speckle pattern, such as highly uniform coverage, sub-micron-sized features and approximately equal speckle size and speckle spacing [49, 50]. These patterns are often applied on silica substrates and remodelled using heat treatments in excess of 300°C; as such, they are not suitable for our requirements.

All coatings were applied using an Agar Scientific Automatic sputter coater with silver and titanium targets (57 mm dia. × 0.1 mm thickness) purchased from Kurt J. Lesker. Welding argon was used as the sputtering gas. The coater
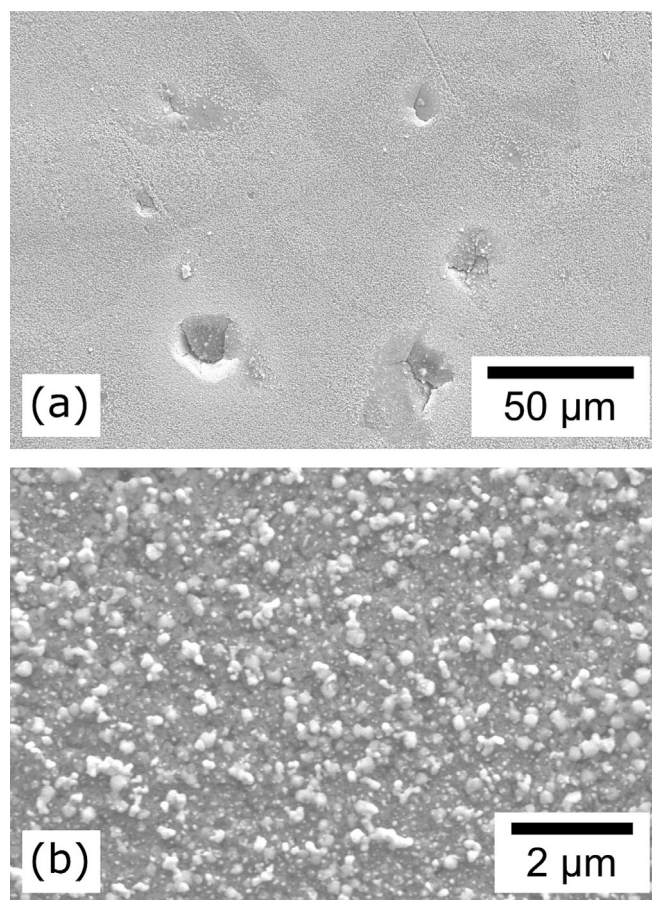
FIGURE 1 Secondary electron images of corroded CuCrZr substrate following patterning with the Ti–Au–Ti–Ag aqueous remodelling methodology of Montgomery et al. [33] showing widespread pitting and loosely adhered surface oxide layers (a) and detail of the corroded specimen surface (b). The initial silver film thickness is 10 nm, remodelling solution is 1 wt.% NaCl in water, and the remodelling time is 120 min.

TABLE 2 Coating parameters used to apply titanium and silver films.

Coating step	Pressure / mbar	Current / mA	Time / s	Thickness / nm
Titanium	0.08	40	300	2–3
Silver	0.08	40	2–10	2–8

chamber was first pumped to a vacuum of 0.01 mbar. The chamber was then flushed with argon gas to remove any residual air. This process was repeated twice before each coating run. Following this, the chamber was pumped to the desired coating pressure. Coating thicknesses were measured using a quartz microbalance thickness monitor. However, this only provides a qualitative thickness measurement. We recommend that any users of this technique perform a sensitivity study to determine the optimum coating parameters for their coating system with these parameters (Table 2) acting as a guide.

Chemical remodelling is the only viable remodelling methodology for sensitive substrates. Silver readily reacts with halogen in solution, with chloride ions in aqueous solution suggested to be the driving force for aqueous silver film remodelling [33, 51, 52]. Sodium salts have various degrees of solubility in alcohols [53], providing a method to produce non-aqueous, halide-containing solutions with readily available laboratory solvents.

Attempts were made to remodel 10 nm silver films with a 1 wt.% NaCl in methanol solution, analogous to the NaCl in water solution in [33], but significant corrosion of the copper substrate occurred. NaCl requires a highly polar solvent to dissolve, and accordingly replacing the NaCl with NaBr (99.97% purity, Fisher Scientific) was required to use milder isopropanol as the solvent. The higher solubility of NaBr in the weakly polar isopropanol allowed us to achieve a
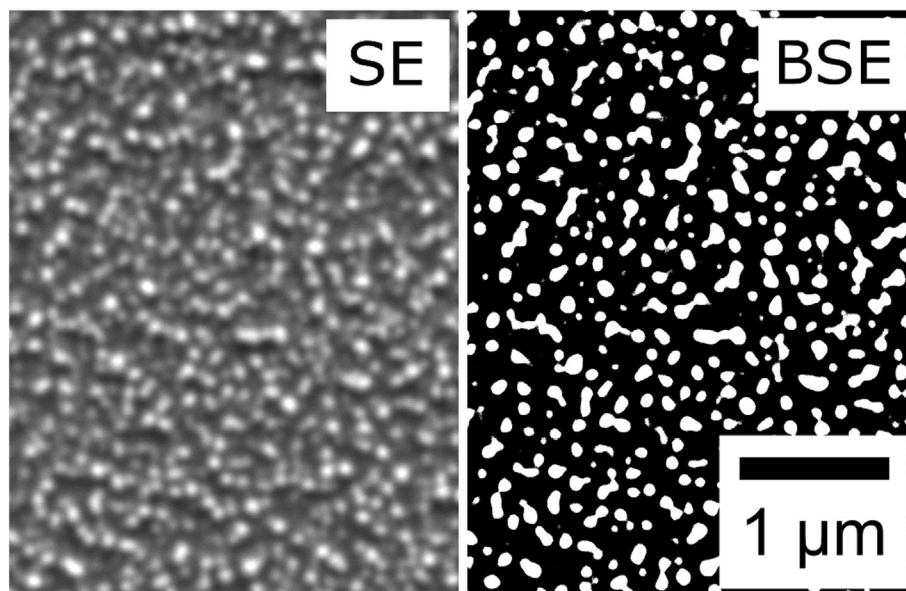
FIGURE 2 Secondary and backscattered electron images of pattern produced from a 3 nm Ti underlayer, 8 nm Ag top layer and 2 h remodelling.

sufficiently concentrated non-aqueous, halide-containing solvent suitable for silver film remodelling. This modified remodelling solution was found to offer similar performance to the NaCl/H_2O solution proposed by Montgomery et al. [33], with complete film remodelling achieved within 2 h of exposure. The remodelling process was found to be highly reproducible, forming near identical patterns for a given silver film thickness.

4 | PROPERTIES OF THE PATTERN

All images of the speckle were captured using a Zeiss EVO LaB$_6$ SEM with images optimised for digital image correlation (DIC) processing as described in [54]. The resulting pattern is very similar to that presented by Montgomery et al. [33] showing complete remodelling of all silver film thicknesses after 2 h of chemical exposure (Figure 2). The pattern comprises discrete silver islands separated by regions containing no residual silver. Qualitatively, the spacing between neighbouring particles appears slightly larger than the single-particle diameter; while equal spacing to particle diameter is desirable, this is well within the acceptable range.

Further optimisation of the pattern was performed by varying the thickness of the silver coating that was applied onto the Ti underlayer and substrate. Increasing the silver film thickness resulted in a slight increase in the effective particle diameter (Figure 3). However, the primary effect of increasing film thickness appeared to be an increase in the robustness of the individual speckles. For thinner films, the particles appeared to be less discrete, with a softer appearance compared to distinct particles with sharper edges resulting from thicker films. This can be observed from the particle size distributions, where in Figure 3a,b, the distributions are not only shifted to the left indicating smaller particles but also the peak is less clear. In comparison, the size distributions in Figure 3c,d have sharper peaks, corresponding to increased numbers of isolated particles in the backscattered electron images. Surface coverage is relatively low and increases monotonically with increasing film thickness. This results in a pattern with larger interparticle spacings than for a gold remodelled pattern [19]. However, the particles are highly uniformly distributed across the entire substrate surface for all film thicknesses. This control of the speckle pattern size by varying the thickness may be desired in materials that either have fine or coarse grains. The capability to tailor the patterns depending on the microstructure using the previously mentioned vapour remodelling techniques is significantly more challenging.

The pattern shows a high level of surface coverage, showing no sensitivity to the substrate. Speckle morphology and coverage appear to be identical on both the Cu-rich matrix phase and Cr-precipitate phase in CuCrZr (Figure 4). This highlights the benefit of using a titanium intermediate layer to reduce direct interaction between the silver layer and the substrate, minimising the effect of surface energy on pattern development for different phases and materials.
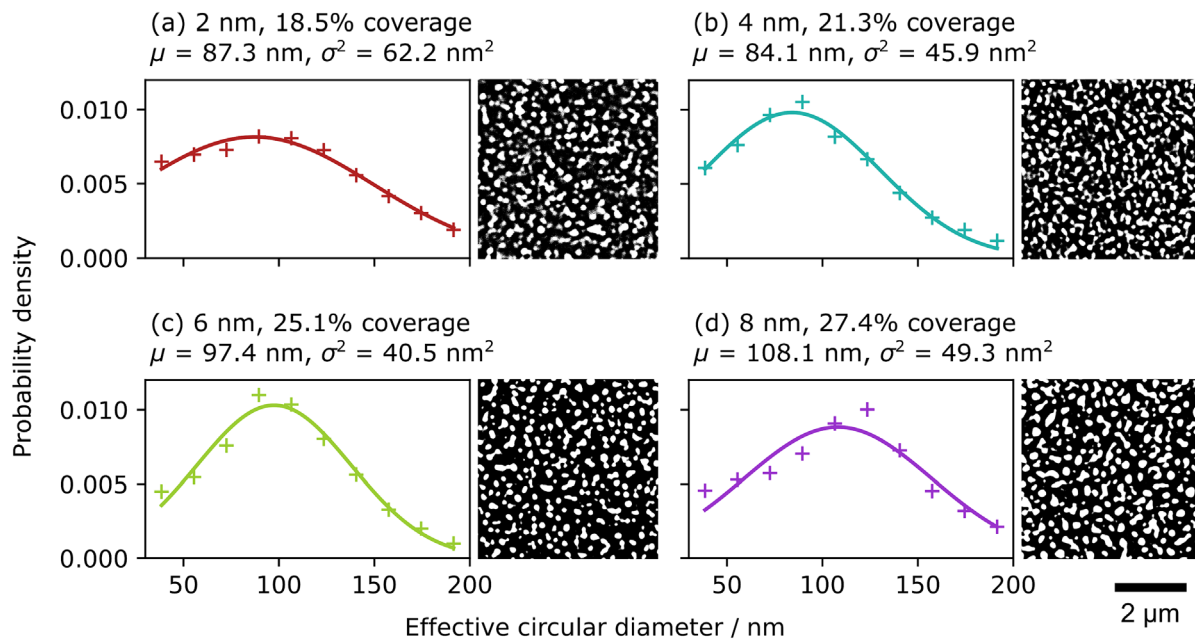
FIGURE 3 Example patterns (backscattered electron images) as a function of Ag layer thickness with the measured particle size distributions, using a Gaussian fit.
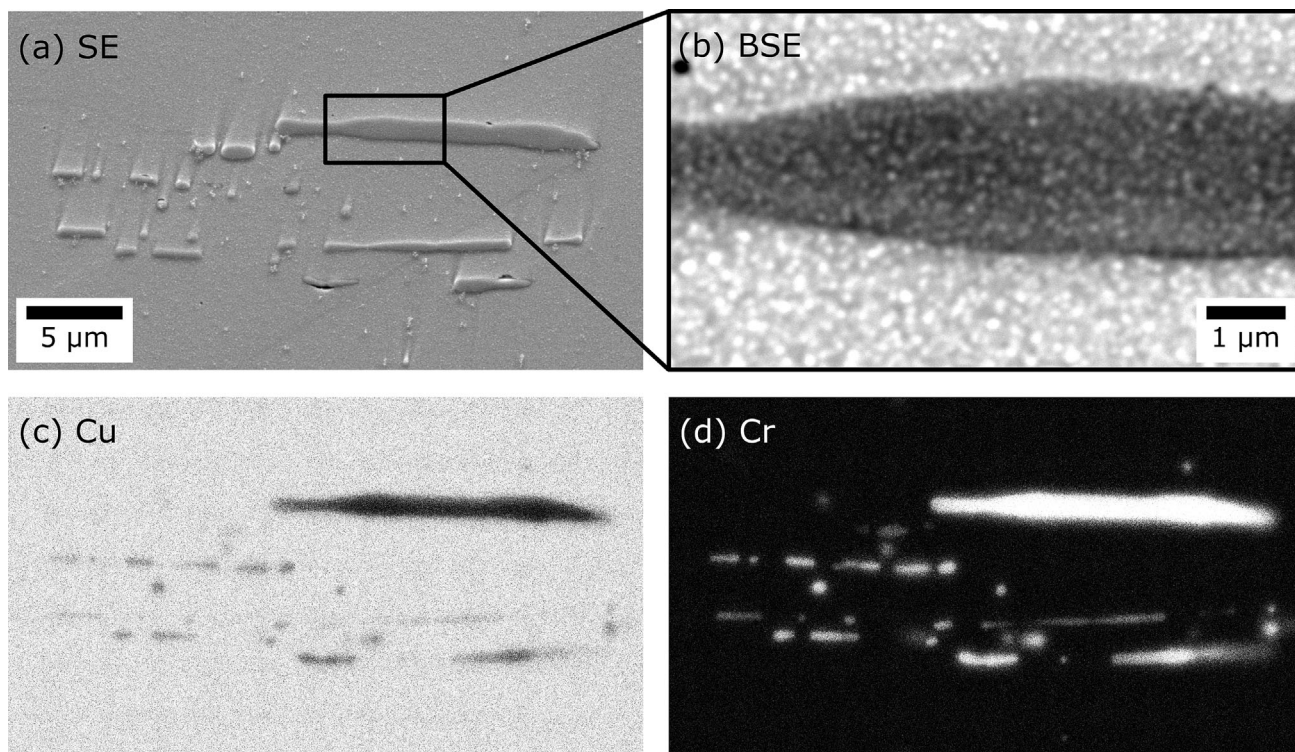

FIGURE 4 Speckle pattern on CuCrZr substrate showing a region containing the copper matrix and chromium-rich precipitates (a, SE image) with a high-magnification image (b, BSE image) showing pattern coverage on both phases. Different levels of z-contrast are observed for the two phases, but the Ag speckles are visible over the entire surface. Elemental maps (qualitative EDX, arbitrary intensity scales) highlight Cu and Cr distributions (c and d, respectively).

4.1 | Orientation mapping through the pattern

HRDIC strain mapping experiments almost invariably require microstructural information acquired through EBSD, and as such, the ability to perform EBSD without pattern removal is a highly useful feature of any patterning technique.

Styrene or water vapour remodelled gold film patterns are the most similar to the silver remodelled pattern discussed here but are not suitable for simultaneous HRDIC and EBSD analysis, limiting their use to post-mortem analysis only [24]. These patterns have the significant disadvantage of requiring mechanical polishing to remove them to conduct EBSD. The polishing removes a thin surface layer of the material of interest, resulting in a mismatch between the microstructure examined with DIC and that measured with post-mortem EBSD. As such, deformation behaviour near to the grain boundaries is difficult to analyse due to the ambiguity in the true grain boundary position. The lack of backscattered electron transparency is likely due to the high atomic number of gold (79) scattering the BSEs as they leave the specimen surface, preventing the formation of resolvable EBSD patterns (EBSPs).

As an alternative to removing the pattern, we found that the silver particles have sufficient electron transparency when using the correct beam conditions to allow for EBSD measurements. Standard conditions for EBSD (Zeiss EVO 10 SEM, Oxford Instruments Symmetry EBSD camera, 20 keV beam energy, 10 nA probe current) were sufficient to produce high-quality EBSPs suitable for orientation measurement (example patterns in Figure 5b). A slight increase in noise is visible, particularly towards the edges of the EBSP but bands and zones are clearly visible. Measures of EBSP quality are given in Table 3, showing a slight degradation in band contrast and mean angular deviation for identical
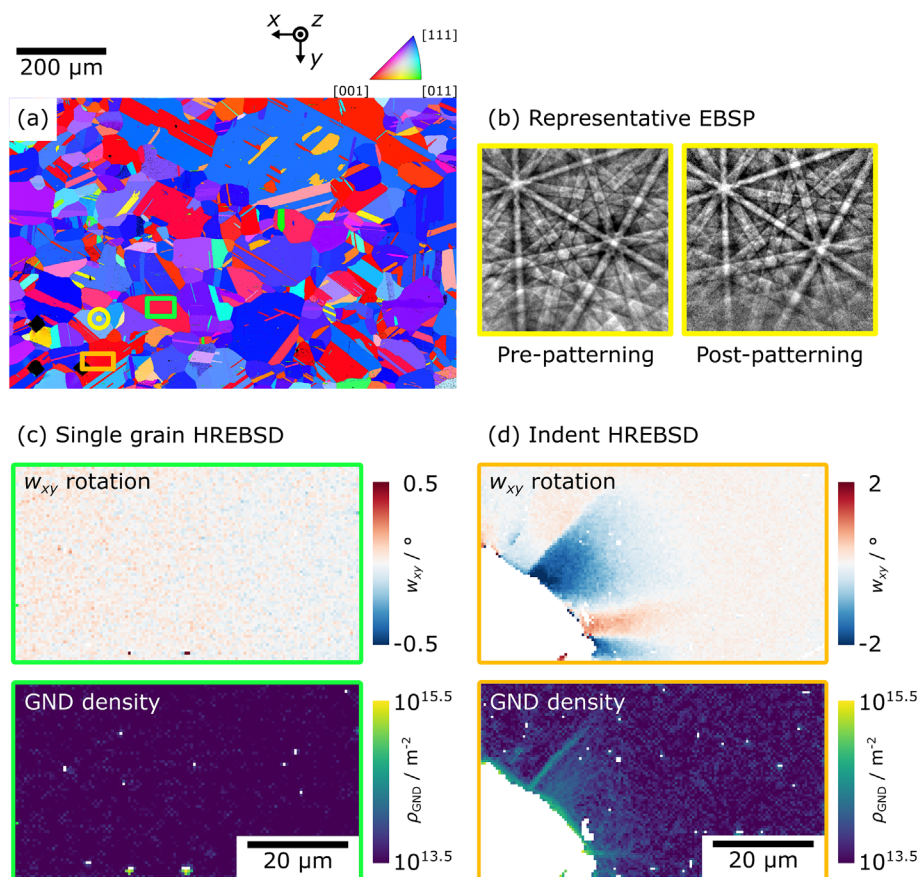
FIGURE 5 EBSD analysis of the effect of pattern application. Pattern quality measurements were obtained for the map presented in (a) with detailed analyses performed on small areas within this region. Sample EBSPs (b) were taken at the point marked with the yellow target under identical conditions (20 kV). HREBSD analyses were performed in the green (c) and orange (d) regions, to examined deformation-free and deformed areas, respectively, following the application of the speckle pattern. The points without values in the rotation and GND density maps are due to chromium precipitates.

conditions following patterning. Increasing the accelerating voltage to 25 kV improved the band contrast but had no significant effect on MAD.

Cross-correlation-based high-angular resolution EBSD (HREBSD) [55–57] requires high-quality EBSPs containing sufficiently fine detail to successfully measure elastic strain, lattice rotations and geometrically necessary dislocation density. Two regions of the map in Figure 5a were re-examined for HREBSD analysis, to test the viability of this technique following HRDIC patterning: one region within a single large grain without deformation and a second region adjacent to a fiducial microhardness indent to examine a deformed region. EBSPs were captured using beam conditions of 20 kV accelerating voltage and 10 nA probe current. An exposure time of 4.2 ms, integrating 10 frames and 2×2 camera binning (622×512 px pattern resolution) gave high-quality patterns suitable for cross-correlation. CrossCourt 4.5.3 was used to perform the analysis, using thirty 128×128 px correlation subwindows with a single manually selected reference pattern for each grain. A step size of 500 nm was used throughout. For the non-deformed region, the reference was chosen in the centre of the region, while for the deformed region, references were chosen sufficiently far from the microhardness indent to be strain free.

The non-deformed, single grain region (Figure 5c) is an estimate of the measurement error due to the speckle pattern since the region is free of deformation. No significant in-plane rotations or GND densities were measured, with the root mean square w_{xy} rotation of 0.06° and the mean GND density of 2.2×10^{13} m^{-2}. These values are similar to those reported in single-crystal silicon [58], demonstrating that the presence of the pattern has minimal impact on the sensitivity of HREBSD. Rotation and GND fields surrounding the hardness indent (Figure 5d) are well captured, showing bands of increased GND density at the interfaces of areas of opposing lattice rotation.

The DIC speckles were not observed in any of the standard EBSP quality metrics. Maps of band contrast, band slope and mean angular deviation were entirely uniform for the region shown in Figure 5c and showed only slight reductions in the areas displaying higher levels of deformation in the region shown in Figure 5d. Cross-correlation quality metrics displayed a similar trend; no discernible effects of the DIC pattern were detected in the cross-correlation peak height or cross-correlation-based kernel average misorientation maps.

As such, the presence of the pattern does not present a barrier to HREBSD analysis, facilitating its HRDIC and HREBSD analysis within the same experiment without the need to remove the pattern. We hypothesise that the lower atomic number of silver (47) allows sufficient BSEs to escape the surface unimpeded, producing high-quality EBSPs. The relatively low surface coverage of the particles is likely to also contribute to this effect.

Other EBSD-compatible patterns exist in the literature, but these often rely on a different patterning technique to thin metal film remodelling. Electron-beam deposition for platinum patterns has been successfully used for simultaneous HRDIC and high-angular resolution EBSD studies in TiAl micropillars [59] and tungsten microcantilevers [60]. While capable of high-resolution strain mapping, this technique can only pattern areas of several tens of square microns, precluding its use from the study of large grained polycrystalline materials such as the Cu-base alloys examined here.

Silica nanoparticle patterning techniques (colloidal silica directly deposited on the surface by Yan et al. [44] and Tasan et al. [61] or by micro-mist nebulisation by Shafqat and Hoefnagels [24]) are suitable for large-area strain mapping with simultaneous EBSD. The low atomic mass and small, amorphous nature of the patterns causes low levels of distortion to EBSPs. However, the relatively low density of speckles limits the spatial resolution of the resulting strain maps.

Microstamping of high-energy electron-transparent urethane patterns using electron-beam lithography produce stamps has been successfully applied on multiple materials to allow complementary EBSD and DIC measurements [62–64]. Ruggles et al. [62] found these patterns to have little effect on HREBSD while Adams et al. [64] have used these patterns to perform near simultaneous HREBSD and DIC in a tilted configuration using the forescatter diodes for

TABLE 3 Values of EBSD map quality and mean angular deviation (MAD) pre- and post-patterning.

Measurement	Pre-patterning (20 kV)	Post-patterning (20 kV)	Post-patterning (25 kV)
Band contrast	107	89	118
Band slope	151	167	138
MAD / °	0.38	0.61	0.66

Note: These measurements are taken from the map presented in Figure 5.

imaging. However, the spatial resolution of microstamp patterns is of the order of several microns owing to the larger feature size.

Electron-beam lithography-based techniques [23, 24, 65, 66] have also been found to be EBSD compatible depending on the Z-number of the deposited pattern. However, these techniques are often low density and limited to small areas, requiring specialist equipment and complicated procedures.

The recent work of Yamasaki et al. [11] applied silver nanoparticles suspended in ethanol to form a speckle pattern with a feature size of approximately 30 nm and a DIC strain spatial resolution of 400 nm. In this study, multiple DIC strain maps and HREBSD stress maps were acquired with increasing applied tensile deformation, allowing the calculation of microscopic, spatially resolved stress–strain curves at distinct deformation features. To the best of our knowledge, this is the highest reported DIC strain mapping resolution coupled with EBSD in the literature.

For all speckle patterning techniques compatible with EBSD, a balance must be struck between spatial resolution of the strain mapping and degradation of the EBSD data quality. Patterns that have the least effect on EBSD data quality tend to have larger or more sparse features, limiting DIC resolution. For the pattern described in this study, the balance is towards high-resolution strain mapping with a slight compromise in EBSD data quality, as shown in the metrics in Table 3. However, the reduction in EBSD data quality is tolerable in that it does not adversely affect HREBSD strain mapping measurements.

If there is a need to fully remove the pattern for further analysis of the specimen, the pattern can be easily removed with an acetone-soaked cotton wool. While this is more damage prone than the chemical depatterning technique possible with functionalised gold nanoparticles [3], mechanical polishing is not necessary.

5 | SUITABILITY OF PATTERNING FOR HRDIC-BASED STRAIN MEASUREMENT

To demonstrate the utility of the patterning methodology, we perform full-field strain mapping of peak-aged CuCrZr when deformed in uniaxial tension. Full heat treatment details are given in [67]. In the peak-aged condition, a 2 h heat treatment at 480°C produces a fine dispersion of 2–3 nm size Cr-rich precipitates in a copper matrix. To ensure sufficient chromium concentration in the matrix phase to form, the zirconium mass fraction exceeds the solubility limit in copper, forming micron-sized body-centred cubic Cr-rich precipitates as shown in Figure 4.

5.1 | Methodology

A tensile dog bone specimen was electric discharge machined from a larger block, with the recast layer removed following machining. The front surface of the specimen was prepared following the route described in Table 1, leaving a flat, deformation-free surface suitable for EBSD analysis and patterning application. A region of interest (ROI) was marked with 40-μm-wide microhardness indents, a sufficient distance from the ROI to ensure that they did not influence strain measurements.

All SEM analyses were performed using the same Zeiss EVO 10 SEM with an Oxford Instruments Symmetry EBSD camera. Pre-deformation EBSD mapping (20 kV beam high tension, 10 nA probe current, 30 μm final aperture, 200 nm step size) was performed over a 500 × 400 μm region, capturing a range of microstructural features, including annealing twins and Cr-rich precipitates, as shown in Figure 6.

The specimen was then patterned using the process described in Section 3.2, applying a 3 nm layer of titanium followed by a 5 nm layer of silver. The silver film was remodelled for 2 h in a 1 wt.% NaBr solution in isopropanol, forming speckles 50–80 nm in diameter with a 20% surface coverage (Figure 7).

BSE imaging for HRDIC was performed using the optimised parameters discussed in [54], using a 20 kV accelerating voltage, 1 nA beam current and a 20 μm aperture. A four-diode, solid-state backscattered electron detector was used for imaging. A grid of 35-μm-wide images with a 2048 × 1536 px resolution and 20% image overlap, covering the central 400 μm × 300 μm section of the ROI, was captured prior to deformation and following each deformation step. The Oxford Instruments large-area mapping tool was used to capture images, using the stage z-coordinate to control focus. The Grid/Collection Stitching plugin within ImageJ was used to form large montage images [68]. DIC was performed using LaVision DaVis 10.0.5 using the FFT-based cross-correlation algorithm. Subwindow size was optimised as in [54], using a 50% subwindow overlap and 272 nm, 16 × 16 px subwindow size. This resulted in a 136 nm strain mapping
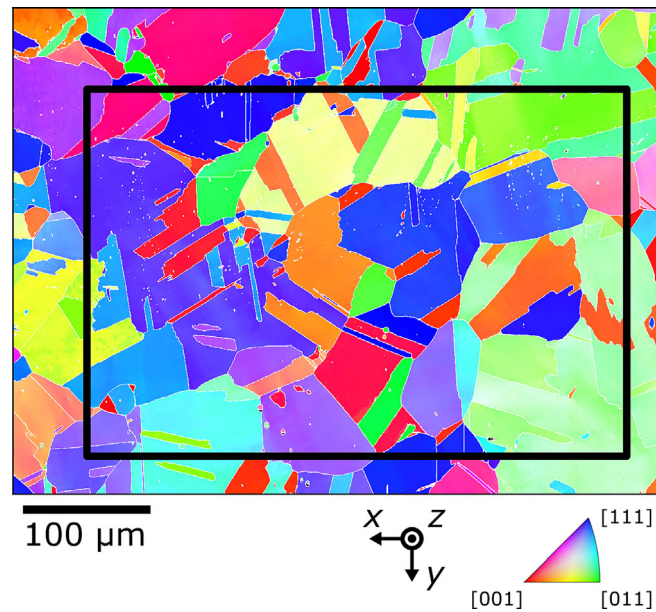
FIGURE 6 Orientation mapping of region of interest, displaying orientations parallel to the x-direction. The black window denotes the HRDIC strain mapping area.
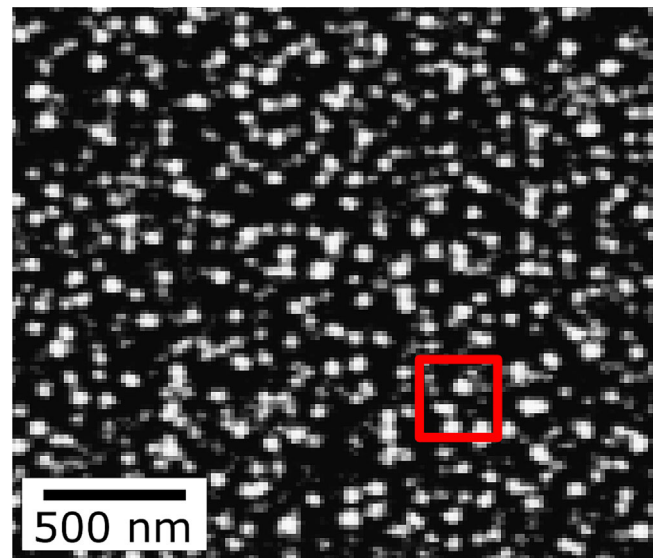
FIGURE 7 Detail of pattern, showing size of DIC subwindow (272 nm) in red.

spatial resolution. The DefDAP python package (v0.93) [69] was used to calculate strains from the displacement field output from DaVis and to register HRDIC strain maps to EBSD orientation measurements. DIC parameters are summarised in Table 4.

Deformation was applied ex situ using an Instron 5966 testing machine under a nominal strain rate of 10^{-3} s^{-1} to plastic strains of 1.0% and 1.5% based on crosshead displacement (Figure 8). The specimen was removed from the testing machine and returned to the SEM for imaging between deformation steps. As such, all strain maps were captured in the non-loaded condition.

TABLE 4 Summary of DIC parameters.

| Parameter	Value
Software	LaVision Davis 10.0.5
Subset size	16 px × 16 px
Subset overlap	50%
Correlation algorithm	2D DIC, fast Fourier transform, reducing window size
Tile field of view	35 μm × 26 μm/2048 px × 1536 μm
Montage field of view	400 μm × 300 μm
Image pre-processing	Shift/rotation correction, no smoothing
Capture instrument	Zeiss EVO 10 SEM, HD backscatter detector
Strain field resolution	136 nm
Differentiation method	Second-order accurate central differences
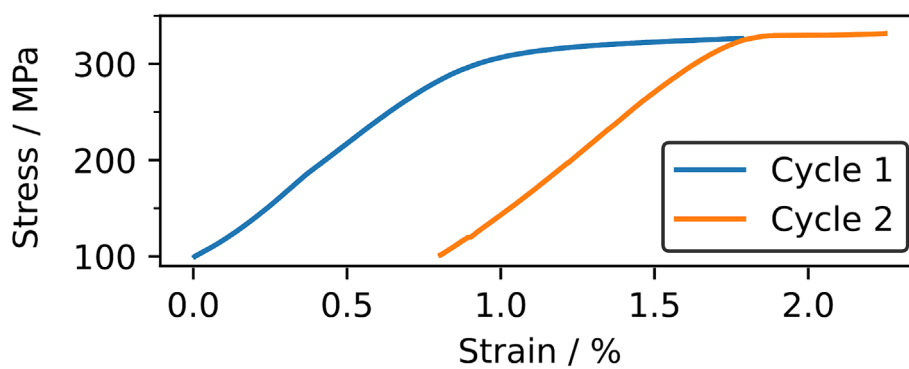
FIGURE 8 Engineering stress strain curves calculated from loadcell output and crosshead displacement. Load and displacement values were recorded every 0.02 s throughout the test.

5.2 | Deformation mapping results

Full-field strain maps following each deformation cycle are shown in Figure 9. Mean strains in the loading direction show good agreement with the target strains applied with crosshead displacement, with 1.0% and 1.4% achieved for the two cycles, respectively.

The maximum in-plane shear strain or effective strain, E_{eff}, is displayed here due to the high level of shear generated by dislocation mediated slip [70]. The effective strain is defined as

$$E_{\text{eff}} = \sqrt{\left(\frac{\frac{\partial u_1}{\partial x_1} - \frac{\partial u_2}{\partial x_2}}{2}\right)^2 + \left(\frac{\frac{\partial u_1}{\partial x_2} + \frac{\partial u_2}{\partial x_1}}{2}\right)^2}, \quad (1)$$

where Directions 1 and 2 are the two in-plane directions, with Direction 1 parallel to the loading direction. u and x are displacement and spatial positions, respectively. The 11 and 22 strain components are defined as $E_{11} = \frac{\partial u_1}{\partial x_1}$ and $E_{22} = \frac{\partial u_2}{\partial x_2}$.

Complex strain patterning is observed across the ROI with the microstructure showing a clear influence on strain localisation. Slip patterns begin at the onset of deformation and appear to be fully developed by 1% global strain, with only an increase in overall intensity following the second deformation cycle. Slip bands are relatively diffuse, manifested as tightly packed, low intensity bands across large sections of grains. This effect is likely due to local strain hardening associated with the presence of the chromium nano-precipitates, preventing significant degrees of strain localisation within the matrix. High levels of strain localisation are almost entirely associated with grain boundaries. This appears as shear along the grain boundaries themselves or as high-intensity slip bands impinging on grain boundaries.
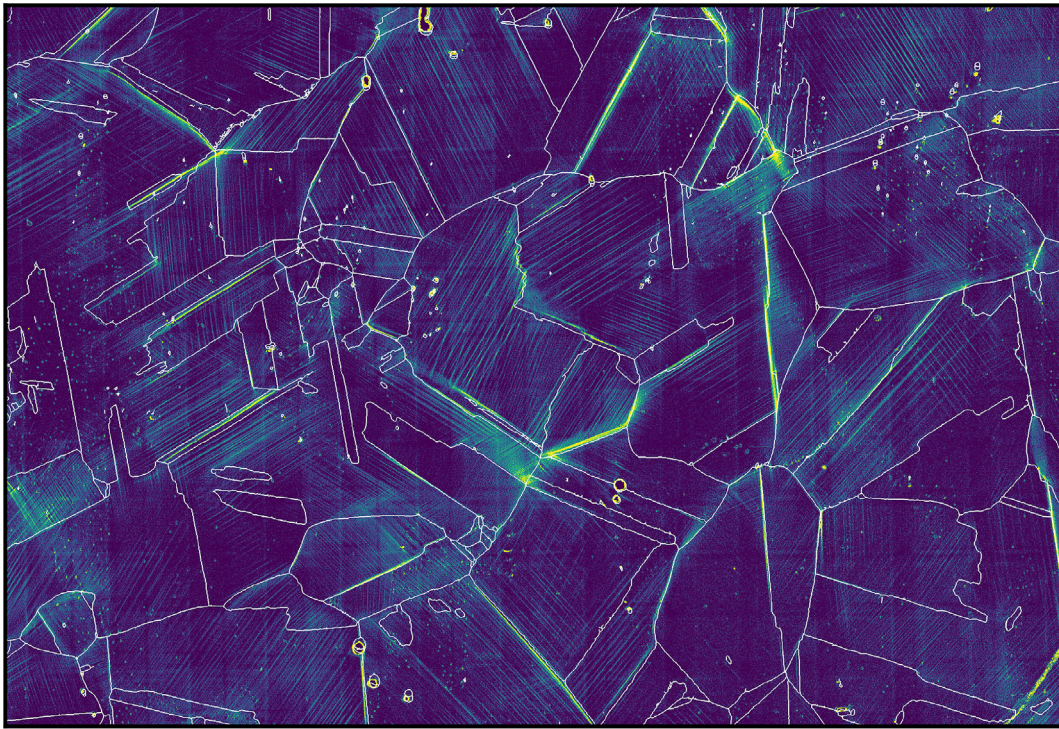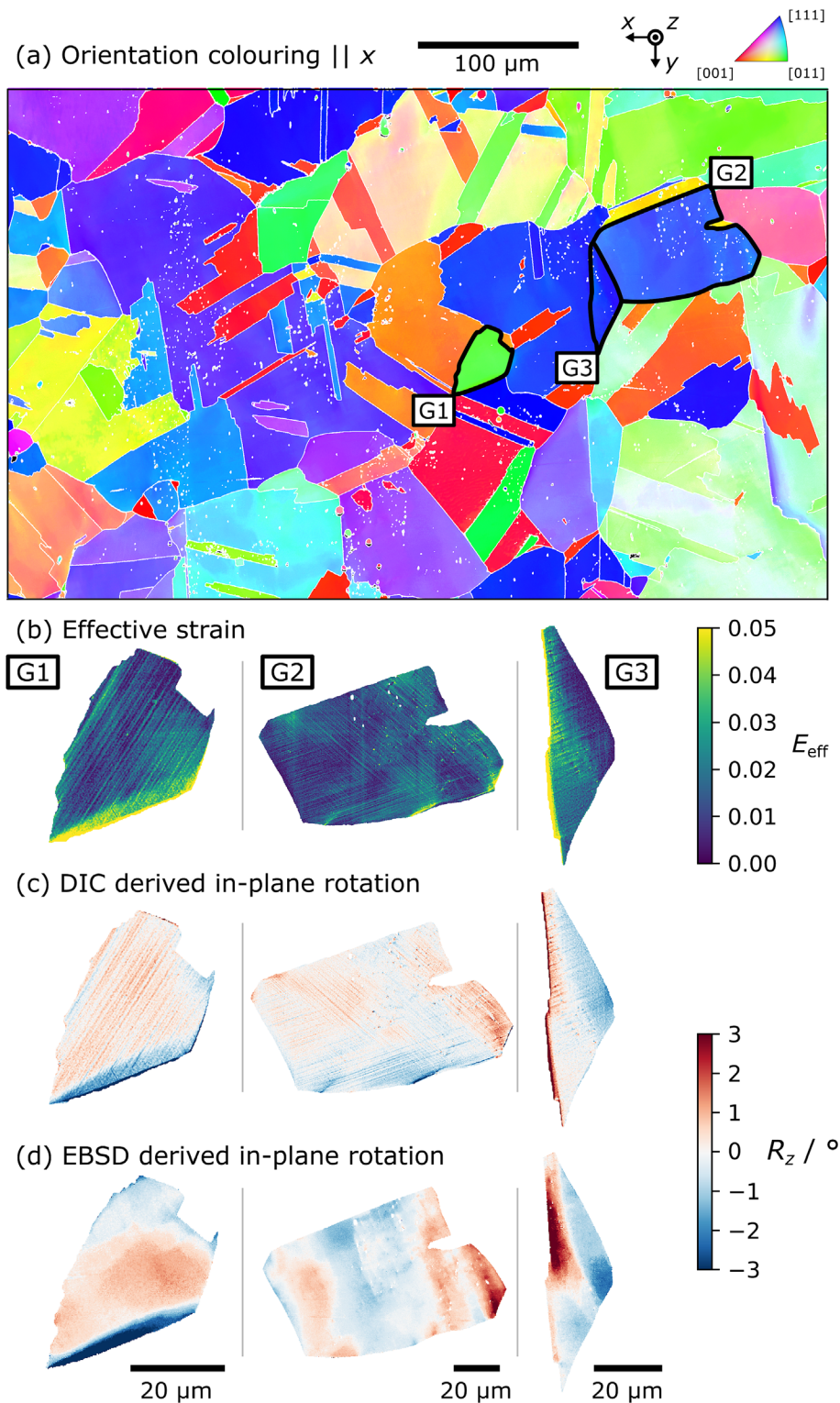
(a) Cycle 1, $\bar{E}_{11}$ = 1.0 %
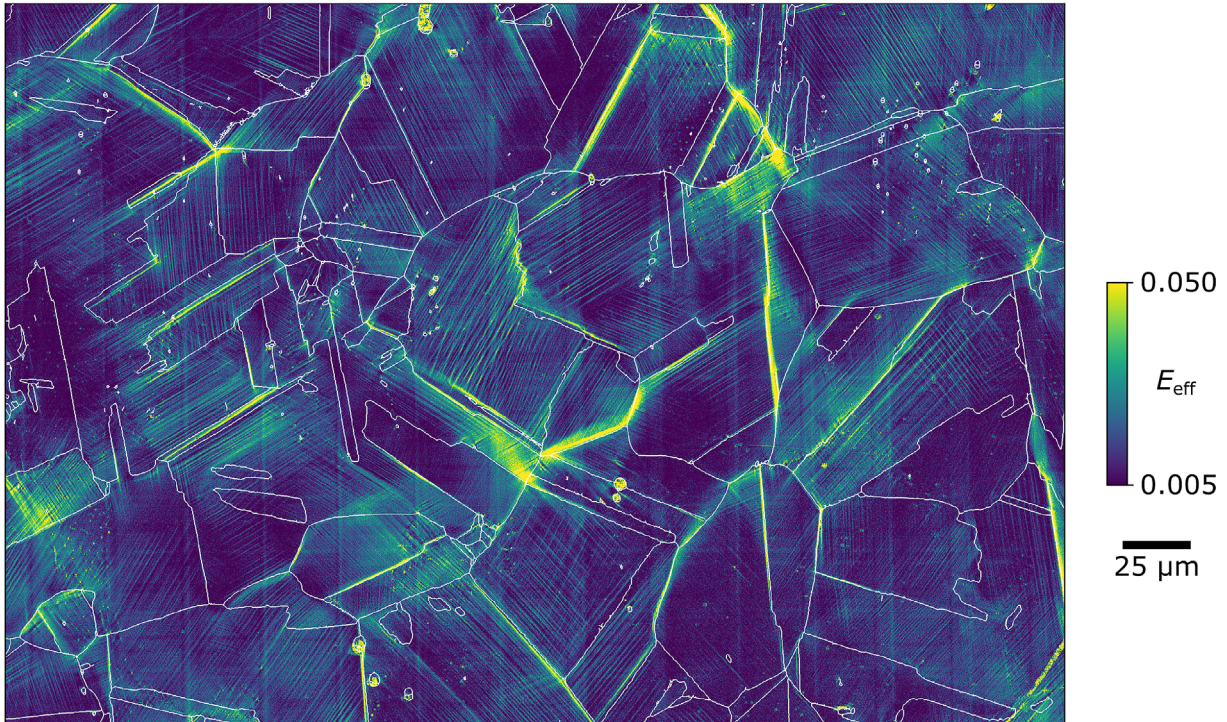
(b) Cycle 2, $\bar{E}_{11}$ = 1.4 %

FIGURE 9 Full-field strain maps following each cycle of deformation. The effective strain measure is shown here. EBSD-determined grain boundaries are shown in white. The loading direction (Direction 1) is the horizontal direction in this figure.

FIGURE 10 Post-deformation EBSD analyses. Orientations parallel to the x-direction are shown in (a). Three grains of interest have been selected to show relations between effect strain (b) and in-plane rotation as measured by DIC relative to the grain average rotation and lattice rotations measured with EBSD (c), where R_z is the in-plane rotation about the z-axis, relative to the grain average orientation. All EBSD measurements are recorded without the removal of the pattern.

The larger micron-sized chromium-rich precipitates do not appear to have a significant effect on strain localisation. EBSD can detect the larger of these precipitates, and these are visible in the grain boundary overlays in Figure 9. However, no strain localisation associated with these features is observed. This may be a result of the relatively low global strains applied here.

All of these deformation features are readily resolved with the speckle pattern, with no apparent artefacts from the patterning process, such as surface oxide cracking (as observed, e.g., in [19]). The pattern remains well adhered to the substrate surface throughout the test with no observed degradation in pattern quality with deformation. A more thorough assessment of the errors and uncertainties associated with HRDIC strain mapping using this pattern and a LaB_6 SEM are presented in [54].

Post-deformation EBSD orientation measurements are presented in Figure 10. Lattice rotations due to deformation can be observed throughout the ROI, visible as non-uniform colouring in the orientation colour map (Figure 10a). As a demonstration of the utility of post-deformation EBSD measurement through the pattern, we present comparisons of HRDIC-derived strain measurements (Figure 10b) and EBSD-derived in-plane rotation measurements (Figure 10c). Three gains of differing slip character were examined.

G1 displays single, planar slip, with slip bands impinging on a straight grain boundary. A plume of strain in the lower part of the grain is clearly visible in the effective strain map (Figure 10b), related to the grain boundary sliding observed in Figure 9. This corresponds to a high large lattice rotation measured by EBSD (Figure 10c).

Multiple slip system activation is visible in many grains throughout the ROI. G2 demonstrates spatially varying slip system activation and slip band intensity, related to the early stages of grain break up. The corresponding EBSD rotation map shows the formation of corresponding cells of opposing lattice rotation. However, a one-to-one correspondence between the two rotation measures is not observed in the case of multiple slip system activation. This apparent mismatch is related to the generation of misorientations through the lattice, continuum rotations due to heterogeneous deformation and the need to maintain compatibility between differentially deforming domains within grains. This effect has been reported in both austenitic stainless steels [13] and in zircaloy-4 following tensile deformation [20].

Finally, G3 displays a high rotation gradient over a relatively narrow grain, corresponding with both grain boundary sliding and slip activation on the left-hand side of the grain and the apparent absence of plasticity in the right-most part of the grain. This demonstrates the generation of significant misorientations through rigid body rotation, owing to plasticity being localised to the left of the grain.

This preliminary study in CuCrZr demonstrates that this patterning methodology is suitable for studying the deformation behaviour associated with metal plasticity. The ability to capture EBSD orientation measurements without the need to remove the pattern allows for complementary rotation measurements to be correlated with HDRIC-based strain and displacement measurements. This study also reveals the complex strain localisation behaviour in CuCrZr, in particular the high level of grain boundary localisation. As such, further study of this material is required to fully understand these deformation phenomena but is beyond the scope of this work.

6 | CONCLUSIONS

The patterning methodology we present here has been shown to be robust under testing, showing no degradation during tensile testing, and demonstrated to be compatible with temperature and corrosion sensitive Cu-base materials. High-quality patterns with a high level of reproducibility can be produced using this method, which requires only a sputter coater and readily available chemical reagents.

The patterns resulting from this methodology are sufficiently refined to allow sub-micron strain mapping, as demonstrated in CuCrZr under tensile loading with strain mapping at a spatial resolution of 136 nm. This is sufficient to readily characterise deformation phenomena such as grain boundary strain localisation and to resolve closely packed, low intensity slip bands resulting from the presence of Cr nano-precipitates.

The EBSD compatibility of this HRDIC pattern allows for crystallographic orientation and rotation measurements to be extracted without removal of the pattern. This allows for a more direct comparison between EBSD- and HRDIC-derived data and a simplified experimental procedure. Comparisons between EBSD- and HRDIC-derived rotation data show the relative contributions to misorientation from rigid body rotation and crystallographic slip, demonstrated here using several characteristic deformation behaviours in CuCrZr. This information could provide further insight into the deformation kinematics of engineering alloys, while providing quantitative information for the calibration of representative crystal scale models.

DATA AVAILABILITY STATEMENT

The data associated with this paper have been made available for public access via the UKAEA Open Data Register and can be accessed at https://doi.org/10.14468/dgzy-j018.

ORCID

Benjamin Poole https://orcid.org/0000-0002-4800-038X

REFERENCES

[1] J. C. Stinville, M. A. Charpagne, R. Maaß, H. Proudhon, W. Ludwig, P. G. Callahan, F. Wang, I. J. Beyerlein, M. P. Echlin, T. M. Pollock, *Annu. Rev. Mat. Res.* **2023**, *53*, 275. https://doi.org/10.1146/annurev-matsci-080921-102621

[2] D. Lunt, R. Thomas, M. D. Atkinson, A. Smith, R. Sandala, J. Q. da Fonseca, M. Preuss, *Acta Mater.* **2021**, *216*, 117111. https://doi.org/10.1016/j.actamat.2021.117111

[3] R. Sperry, S. Han, Z. Chen, S. H. Daly, M. A. Crimp, D. T. Fullwood, *Mater Charact* **2021**, *173*, 110941. https://doi.org/10.1016/j.matchar.2021.110941

[4] R. Sperry, A. Harte, J. Quinta da Fonseca, E. R. Homer, R. H. Wagoner, D. T. Fullwood, *Acta Mater.* **2020**, *193*, 229. https://doi.org/10.1016/j.actamat.2020.04.037

[5] A. Harte, M. Atkinson, A. Smith, C. Drouven, S. Zaefferer, J. Quinta da Fonseca, M. Preuss, *Acta Mater.* **2020**, *194*, 257. https://doi.org/10.1016/j.actamat.2020.04.004

[6] J. C. Stinville, M. P. Echlin, D. Texier, F. Bridier, P. Bocher, T. M. Pollock, *Exp. Mech.* **2016**, *56*, 197. https://doi.org/10.1007/s11340-015-0083-4

[7] M. A. Charpagne, J. M. Hestroffer, A. T. Polonsky, M. P. Echlin, D. Texier, V. Valle, I. J. Beyerlein, T. M. Pollock, J. C. Stinville, *Acta Mater.* **2021**, *215*, 117037. https://doi.org/10.1016/j.actamat.2021.117037

[8] A. D. Kammers, S. Daly, *Exp. Mech.* **2013**, *53*, 1333. https://doi.org/10.1007/s11340-013-9734-5

[9] A. Bergsmo, Y. Xu, B. Poole, F. P. Dunne, *J. Mech. Phys. Solids* **2022**, *160*, 104785. https://doi.org/10.1016/j.jmps.2022.104785

[10] R. Jiang, F. Pierron, S. Octaviani, P. A. S. Reed, *Mater. Sci. Eng. A* **2017**, *699*, 128. https://doi.org/10.1016/j.msea.2017.05.091

[11] S. Yamasaki, H. Matsuo, T. Morikawa, M. Tanaka, *Scr. Mater.* **2023**, *235*, 115603. https://doi.org/10.1016/j.scriptamat.2023.115603

[12] A. W. Mello, A. Nicolas, M. D. Sangid, *Mater. Sci. Eng. A* **2017**, *695*, 332. https://doi.org/10.1016/j.msea.2017.04.002

[13] F. Di Gioacchino, J. Quinta da Fonseca, *Int. J. Plast.* **2015**, *74*, 92. https://doi.org/10.1016/j.ijplas.2015.05.012

[14] B. Poole, F. P. E. Dunne, *Mater. Sci. Eng. A* **2021**, *813*, 141176. https://doi.org/10.1016/j.msea.2021.141176

[15] T. Vermeij, J. Hoefnagels, *Scr. Mater.* **2022**, *208*, 114327. https://doi.org/10.1016/j.scriptamat.2021.114327

[16] T. Vermeij, J. A. C. Verstijnen, T. J. J. R. y. Cantador, B. Blaysat, J. Neggers, J. P. M. Hoefnagels, *Exp. Mech.* **2022**, *62*, 1625. https://doi.org/10.1007/s11340-022-00884-0

[17] Q. Shi, S. Roux, F. Latourte, F. Hild, D. Loisnard, N. Brynaert, *Ultramicroscopy* **2018**, *184*, 71. https://doi.org/10.1016/j.ultramic.2017.08.005

[18] S. Isavand, A. Assempour, *Int. J. Mech. Sci.* **2021**, *200*, 106441. https://doi.org/10.1016/j.ijmecsci.2021.106441

[19] D. Lunt, A. Orozco-Caballero, R. Thomas, P. Honniball, P. Frankel, M. Preuss, J. Quinta da Fonseca, *Mater Charact* **2018**, *139*, 355. https://doi.org/10.1016/j.matchar.2018.03.014

[20] R. Thomas, D. Lunt, M. D. Atkinson, J. Quinta da Fonseca, M. Preuss, F. Barton, J. O'Hanlon, P. Frankel, *Dent. Mater.* **2019**, *5*, 100248. https://doi.org/10.1016/j.mtla.2019.100248

[21] M. A. Charpagne, J. C. Stinville, F. Wang, N. Philips, T. M. Pollock, *Mater. Sci. Eng. A* **2022**, *848*, 143291. https://doi.org/10.1016/j.msea.2022.143291

[22] Z. Ye, C. Li, M. Zheng, X. Zhang, X. Yang, J. Gu, *Int. J. Plast.* **2022**, *152*, 103247. https://doi.org/10.1016/j.ijplas.2022.103247

[23] Y. L. Dong, B. Pan, *Exp. Mech.* **2017**, *57*, 1161. https://doi.org/10.1007/s11340-017-0283-1

[24] S. Shafqat, J. P. M. Hoefnagels, *Exp. Mech.* **2021**, *61*, 917. https://doi.org/10.1007/s11340-020-00686-2

[25] A. Orozco-Caballero, D. Lunt, J. D. Robson, J. Quinta da Fonseca, *Acta Mater.* **2017**, *133*, 367. https://doi.org/10.1016/j.actamat.2017.05.040

[26] F. Di Gioacchino, J. Quinta da Fonseca, *Exp. Mech.* **2013**, *53*, 743. https://doi.org/10.1007/s11340-012-9685-2

[27] A. Githens, S. Daly, *Strain* **2017**, *53*, e12215. https://doi.org/10.1111/str.12215

[28] J. G. Byrne, M. E. Fine, A. Kelly, *Philos. Mag. J. Theor. Exp. Appl. Phys.* **1961**, *6*, 1119. https://doi.org/10.1080/14786436108239674

[29] G. M. Kalinin, S. A. Fabritziev, B. N. Singh, S. Tahtinen, S. J. Zinkle, *J. Nucl. Mater.* **2002**, *307–311*, 668. https://doi.org/10.1016/S0022-3115(02)01185-6

[30] T. Gu, V. S. Tong, C. M. Gourlay, T. B. Britton, *Acta Mater.* **2020**, *196*, 31. https://doi.org/10.1016/j.actamat.2020.06.013

[31] T. Gu, Y. Xu, C. M. Gourlay, T. B. Britton, *Scr. Mater.* **2020**, *175*, 55. https://doi.org/10.1016/j.scriptamat.2019.09.003

[32] Y. Xu, T. Gu, J. Xian, F. Giuliani, T. Ben Britton, C. M. Gourlay, F. P. E. Dunne, *Int. J. Plast.* **2021**, *137*, 102904. https://doi.org/10.1016/j.ijplas.2020.102904

[33] C. B. Montgomery, B. Koohbor, N. R. Sottos, *Exp. Mech.* **2019**, *59*, 1063. https://doi.org/10.1007/s11340-019-00487-2

[34] V. R. Barabash, G. M. Kalinin, S. A. Fabritsiev, S. J. Zinkle, *J. Nucl. Mater.* **2011**, *417*, 904. https://doi.org/10.1016/j.jnucmat.2010.12.158

[35] K. Zhang, E. Gaganidze, M. Gorley, *Fusion Eng. Des.* **2019**, *144*, 148. https://doi.org/10.1016/j.fusengdes.2019.04.094

[36] J. H. You, E. Visca, T. Barrett, B. Böswirth, F. Crescenzi, F. Domptail, M. Fursdon, F. Gallay, B.-E. Ghidersa, H. Greuner, M. Li, A. V. Müller, J. Reiser, M. Richou, S. Roccella, C. H. Vorpahl, *Nucl. Mater. Energy* **2018**, *16*, 1. https://doi.org/10.1016/j.nme.2018.05.012

[37] G. Kalinin, R. Matera, *J. Nucl. Mater.* **1998**, *258–263*, 345. https://doi.org/10.1016/S0022-3115(98)00271-2

[38] F. Crescenzi, C. Bachmann, M. Richou, S. Roccella, E. Visca, J.-H. You, *Fusion Eng. Des.* **2015**, *98–99*, 1263. https://doi.org/10.1016/j.fusengdes.2015.02.056

[39] G. M. Kalinin, A. D. Ivanov, A. N. Obushev, B. S. Rodchenkov, M. E. Rodin, Y. S. Strebkov, *J. Nucl. Mater.* **2007**, *367–370*, 920. https://doi.org/10.1016/j.jnucmat.2007.03.256

[40] *A Good Practices Guide for Digital Image Correlation* (Eds: International Digital Image Correlation Society, E. M. C. Jones, M. A. Iadicola). **2018**. https://doi.org/10.32720/idics/gpg.ed1

[41] T. E. J. Edwards, F. Di Gioacchino, H. P. Springbett, R. A. Oliver, W. J. Clegg, *Exp. Mech.* **2017**, *57*, 1469. https://doi.org/10.1007/s11340-017-0317-8

[42] J. P. M. Hoefnagels, M. P. F. H. L. van Maris, T. Vermeij, *Strain* **2019**, *55*, e12330. https://doi.org/10.1111/str.12330

[43] S. Fürtauer, D. Li, D. Cupid, H. Flandorfer, *Intermetallics* **2013**, *34*, 142. https://doi.org/10.1016/j.intermet.2012.10.004

[44] D. Yan, C. C. Tasan, D. Raabe, *Acta Mater.* **2015**, *96*, 399. https://doi.org/10.1016/j.actamat.2015.05.038

[45] A. D. Kammers, S. Daly, *Meas. Sci. Technol.* **2011**, *22*, 125501. https://doi.org/10.1088/0957-0233/22/12/125501

[46] J. P. Goulmy, D. Depriester, F. Guittonneau, L. Barrallier, S. Jégou, *Mater Charact* **2022**, *194*, 112322. https://doi.org/10.1016/j.matchar.2022.112322

[47] M. E. Harr, S. Daly, A. L. Pilchak, *Int. J. Fatigue* **2021**, *147*, 106173. https://doi.org/10.1016/j.ijfatigue.2021.106173

[48] J. C. Stinville, T. Francis, A. T. Polonsky, C. J. Torbet, M. A. Charpagne, Z. Chen, G. H. Balbus, F. Bourdin, V. Valle, P. G. Callahan, M. P. Echlin, T. M. Pollock, *Exp. Mech.* **2020**, *61*, 331. https://doi.org/10.1007/s11340-020-00632-2

[49] L.-L. Bao, S. M. Mahurin, C.-D. Liang, S. Dai, *J. Raman Spectrosc.* **2003**, *34*, 394. https://doi.org/10.1002/jrs.993

[50] J. Quan, J. Zhang, X. Qi, J. Li, N. Wang, Y. Zhu, *Sci. Rep.* **2017**, *7*, 14771. https://doi.org/10.1038/s41598-017-15372-y

[51] K. Koike, F. Yamazaki, T. Okamura, S. Fukuda, *J. Vac. Sci. Technol. A* **2007**, *25*, 527. https://doi.org/10.1116/1.2722758

[52] K. Koike, S. Fukuda, *J. Vac. Sci. Technol. A* **2008**, *26*, 444. https://doi.org/10.1116/1.2897315

[53] S. P. Pinho, E. A. Macedo, *J. Chem. Eng. Data* **2005**, *50*, 29. https://doi.org/10.1021/je049922y

[54] B. Poole, A. Marsh, D. Lunt, C. Hardie, M. Gorley, C. Hamelin, A. Harte, *Strain* **2023**. https://doi.org/10.1111/str.12472

[55] A. J. Wilkinson, G. Meaden, D. J. Dingley, *Mater. Sci. Technol.* **2006**, *22*, 1271. https://doi.org/10.1179/174328406X130966

[56] A. J. Wilkinson, G. Meaden, D. J. Dingley, *Ultramicroscopy* **2006**, *106*, 307. https://doi.org/10.1016/j.ultramic.2005.10.001

[57] A. J. Wilkinson, D. J. Dingley, G. Meaden, Strain mapping using electron backscatter diffraction, in *Electron Backscatter Diffraction in Materials Science*, 2nd ed. (Eds: A. J. Schwartz, B. L. Adams, D. P. Field), Springer, New York, NY **2009**.

[58] J. Jiang, T. B. Britton, A. J. Wilkinson, *Ultramicroscopy* **2013**, *125*, 1. https://doi.org/10.1016/j.ultramic.2012.11.003

[59] T. E. J. Edwards, F. Di Gioacchino, G. Mohanty, J. Wehrs, J. Michler, W. J. Clegg, *Acta Mater.* **2018**, *148*, 202. https://doi.org/10.1016/j.actamat.2018.01.007

[60] T. E. J. Edwards, X. Maeder, J. Ast, L. Berger, J. Michler, *Sci. Adv.* **2022**, *8*, eabo5735. https://doi.org/10.1126/sciadv.abo5735

[61] C. C. Tasan, J. P. M. Hoefnagels, M. Diehl, D. Yan, F. Roters, D. Raabe, *Int. J. Plast.* **2014**, *63*, 198. https://doi.org/10.1016/j.ijplas.2014.06.004

[62] T. J. Ruggles, G. F. Bomarito, A. H. Cannon, J. D. Hochhalter, *Microsc. Microanal.* **2017**, *23*, 1091. https://doi.org/10.1017/S1431927617012703

[63] A. W. Mello, A. Nicolas, R. A. Lebensohn, M. D. Sangid, *Mater. Sci. Eng. A* **2016**, *661*, 187. https://doi.org/10.1016/j.msea.2016.03.012

[64] D. Adams, S. Irfan, J. Cramer, M. P. Miles, E. R. Homer, T. Brown, R. K. Mishra, D. T. Fullwood, *Microsc. Microanal.* **2020**, *26*, 641. https://doi.org/10.1017/S1431927620001701

[65] A. Guery, F. Latourte, F. Hild, S. Roux, *Meas. Sci. Technol.* **2013**, *25*, 015401. https://doi.org/10.1088/0957-0233/25/1/015401

[66] S. M. Guo, M. A. Sutton, N. Li, X. D. Li, L. W. Wang, S. Rajan, *Exp. Mech.* **2017**, *57*, 41. https://doi.org/10.1007/s11340-016-0206-6

[67] A. J. Cackett, J. J. H. Lim, P. Klupś, A. J. Bushby, C. D. Hardie, *J. Nucl. Mater.* **2018**, *511*, 610. https://doi.org/10.1016/j.jnucmat.2018.04.012

[68] S. Preibisch, S. Saalfeld, P. Tomancak, *Bioinformatics* **2009**, *25*, 1463. https://doi.org/10.1093/bioinformatics/btp184

[69] M. D. Atkinson, R. Thomas, A. Harte, P. Crowther, J. Quinta da Fonseca, DefDAP: Deformation Data Analysis in Python—v0.92. **2020**. https://doi.org/10.5281/zenodo.3784775

[70] G. E. Dieter, *Mechanical Metallurgy*, McGraw-Hil, New York **1961**.